2

Sn-doped Cobalt Containing Perovskite as the Air Electrode for Highly

Active and Durable Reversible Protonic Ceramic Electrochemical Cells

- 4 Min Fu^a, Wenjing Hu^a, Hua Tong^a, Xin Ling^a, Linggui Tan^a, Fanglin Chen ^{b*} and Zetian Tao^{a*}
- ^a School of Resources, Environment and Safety Engineering, University of South China, Hengyang,
- 6 Hunan Province 421001, China
- ⁷ Department of Mechanical Engineering, University of South Carolina, Columbia, SC, 29208, USA
- * Corresponding author.
- 9 E-mail: newton@mail.ustc.edu.cn, taozetian@usc.edu.cn (Z. Tao) and chenfa@cec.sc.edu (F. Chen)
- 10 Abstract: One potential solution to the problems of energy storage and conversion is the use of
- reversible protonic ceramic electrochemical cells (R-PCEC), which is based on the solid oxide fuel cell
- 12 (SOFC) technology and offers a flexible route to the generation of renewable fuels. However, the R-
- 13 PCEC development faces a range of significant challenges, including slow oxygen reaction kinetics,
- inadequate durability, and poor round-trip efficiency resulted from the inadequacy of the air electrode.
- To address these issues, we report a novel B-sites doped Pr_{0.5}Ba_{0.5}Co_{0.7}Fe_{0.3}O_{3-δ} (PBCF) with varying
- amounts of Sn as the air electrode for R-PCEC to further enhance the electrochemical performance at
- 17 lower temperatures. At 600 °C, the R-PCEC with an air electrode consisting of
- Pr_{0.5}Ba_{0.5}Co_{0.7}Fe_{0.25}Sn_{0.05}O_{3+δ} has achieved a peak power density of 1.12 W cm⁻² in the fuel cell mode
- and a current density of 1.79 A cm⁻² in the electrolysis mode at a voltage of 1.3 V. Moreover, the R-
- 20 PCECs have shown good stability in the electrolysis mode of 100 hours. This study presents a practical
- 21 method for developing durable high-performance air electrodes for R-PCECs.
- 22 Keywords: triple conducting oxide; dual-element doping; protonic ceramic electrochemical cells;
- 23 catalytic

24

1 Introduction

25

26

27

28

29

30

31

32

33

34

35

36

37

38

39

40

41

42

43

44

45

46

47

48

49

Reversible protonic ceramic electrochemical cell (R-PCEC), derived from protonic ceramic fuel cell (PCFC) technology, is a highly efficient energy conversion technology that can convert chemical and electrical energy at medium and low temperatures with great versatility. Recently, there has been a great amount of research conducted on R-PCECs because to its numerous benefits. These include the ability to directly produce dry hydrogen, operate at lower temperatures, and offer significant costcutting opportunities [1-4]. R-PCECs are capable of converting water and carbon dioxide into hydrogen and other valuable carbon-based fuels via electrolysis mode, providing an attractive means of efficient energy storage. Meanwhile, R-PCECs can generate electricity on demand in the fuel cell mode supplementary to other intermittent renewable electricity sources, such as solar and wind power[5-7]. The proton-conducting type oxides as the principal component of the electrolyte can not only ensure good proton conductivity for R-PCEC at low temperatures but also improve the safety and stability of the R-PCEC system. BaZr_{0.1}Ce_{0.7}Y_{0.1}Yb_{0.1}O₃ (BZCYYb) is a BaCeO₃-BaZrO₃-based electrolyte obtained by co-doping with two aliovalent elements at the B-site. This material has been extensively studied and found to exhibit favorable proton and oxygen ion conduction characteristics. As a result, it is widely regarded as the preferred electrolyte material for typical R-PCECs[8-10]. Due to the significant role of oxygen ion and proton conduction in BZCYYb, the simultaneous steam electrolysis from the solid oxide electrolysis cells (SOECs) can be achieved by feeding steam to both sides of the air and fuel electrodes, leading to a notable rise in current density at 1.3V[11, 12]. However, the most important challenge facing the development of R-PCECs is addressing the inadequate performance of the air electrodes during oxygen reduction reaction (ORR, in the fuel cell mode) and oxygen evolution reaction (OER, in the electrolysis mode) at low and medium temperatures. Although mixed oxide-ion/electron-hole conductors (MIECs) exhibit good catalytic activity for ORR in the conventional SOFC with oxygen ion conducting electrolyte, severe degradation

of electrochemical performance occurs when MIECs are used as the air electrode in PCECs[13, 14].

52

54

55

56

57

58

59

60

61

62

63

64

65

66

67

68

69

70

71

72

73

74

50 During fabrication or ORR operation, decomposition of the electrode and chemical reaction with the

electrolyte may arise, which leads to the degradation of electrochemical performance[15]. Therefore,

there is an urgent need to explore new air electrode materials with high catalytic activity and chemical

stability suitable for R-PCEC systems.

To efficiently enlarge the active sites of the reaction, an air electrode material for R-PCECs should be a triple conducting oxide to facilitate the transfer of oxygen ions, electrons, and hydrogen ions. Doping protonic conducting oxides with transition metals to increase their oxygen ion and electron conductivity, such as various multivalent element-doped BaCeO₃ and BaZrO₃, has been suggested as a more promising approach to the creation of the air electrode materials, although low total conductivity still restrains the practical application of these electrodes[16, 17]. The triple phase boundaries (TPB) enhancement of ORR/OER can also be accomplished through a mixture of conventional MIECs and pure protonic conducting oxides, and the mechanism underlying the effect of mixed air electrode micromorphology change on electrochemical performance has been clearly recognized[18, 19]. Furthermore, some MIEC materials, such as La_{0.6}Sr_{0.4}Co_{0.2}Fe_{0.8}O_{3-δ} (LSCF), $Ba_{0.5}Sr_{0.5}Co_{0.8}Fe_{0.2}O_{3-\delta}$ (BSCF), $PrBaCo_2O_{5+\delta}$ (PBCO), and $BaCo_{0.5}Fe_{0.5}O_{3-\delta}$ (BCF), have electrocatalytic activity for proton reactions because of their high oxygen vacancy content[20, 21]. The experimental observation demonstrates that oxygen ions and protons are involved in the electrochemical reaction, as the electrochemical efficiency of these electrode materials is highly dependent on the water pressure. A few cobalt containing perovskites, such as PrBa_{0.5}Sr_{0.5}Co₂O_{5+δ} (PBSC)[22], NdBa_{0.5}Sr_{0.5}Co_{1.5}Fe_{0.5}O_{5+δ} (NBSCF)[23], Ba_{0.9}K_{0.1}Co_{0.4}Fe_{0.4}Zr_{0.2}O_{3-δ} (BKCFZ)[24] and BaCo_{0.4}Fe_{0.4}Zr_{0.1}Y_{0.1}O_{3-δ} (BCFZY)[5] have recently been identified as triple conducting oxides in proton conducting SOFCs or SOECs at intermediate temperatures (600~700 °C). However, the thermal expansion coefficient (TEC) of cobalt based perovskite is relatively high, especially compared to barium cerate based electrolytes, making it difficult to optimize the interface between electrode and electrolyte [25, 26].

As a multivalent element, Sn is an excellent doping choice because it can simultaneously modify the thermal expansion coefficient and boost the catalytic activity of the doped substance, as shown by numerous investigations[27-29]. Sn doping has been found to have a positive effect on the catalytic activity in certain fuel electrode materials, such as Sn doped Ni-GDC and Ni-YSZ[27]. When Sn is doped into the B-site of BaFeO_{3- δ} parent oxide, the resulting BaFe_{0.95}Sn_{0.05}O_{3- δ} material exhibits high efficiency for SOFCs because it stabilizes a single perovskite lattice structure and promotes oxygen reduction activity[30]. In addition, Sn doped Bi_{0.5}Sr_{0.5}FeO_{3- δ} exhibits expanded lattice parameters, resulting in increased r_c and larger average binding energy (ABE) values. Therefore, BSFSn has a smaller TEC than BSF at temperatures between 50 and 800 °C, with an average value of 12.9×10⁻⁶ K⁻¹[31]. It has been demonstrated that the thermal expansion coefficient modified by Sn doping is more closely matched to that of the electrolyte, promoting chemical and structural compatibility between the electrody and electrolyte, lowering interfacial resistance and increasing ORR reactivity.

Herein, we report a perovskite oxide with the potential for proton conduction, Pr_{0.5}Ba_{0.5}Co_{0.7}Fe_{0.3-x}Sn_xO_{3-δ} (x=0.01, 0.03, 0.05, 0.07) named as PBCFS01-07 respectively, as air electrode in R-PCECs with superior ORR activity. Our experimental investigation and density function theory (DFT) calculation demonstrate that proton defect can be easily generated through hydration reaction when Sn is doped in the B-site of Pr_{0.5}Ba_{0.5}Co_{0.7}Fe_{0.3}O_{3-δ} perovskite. Therefore, the B-site substitution of Sn can effectively lower the energy barrier of proton conduction. By facilitating ORR and OER, the triple conduction ability demonstrated by this material improves its electrochemical performance, enabling a reversible operation of the electrochemical cell at temperatures between 500-700 °C.

2 Experimental

The citric acid-nitrate gel combustion technique was utilized in the preparation of both the electrode materials and the electrolyte materials. PBCFS01-07, for instance, is synthesized by dissolving Pr(NO₃)₃·6H₂O, BaCO₃, Co(NO₃)₃·6H₂O, Fe(NO₃)·9H₂O, and SnO in nitric acid solution in stoichiometric proportions, followed by the addition of citric acid at a molar ratio of citric acid/metal

is subjected to dehydration.

ions of 1:1.5. The solution was heated while stirred in order to vaporize water until it changed to a viscous gel and finally self-combusted. The precursors of BZCYYb and anode functional layer (AFL) composed of NiO-BaZr_{0.1}Ce_{0.7}Y_{0.1}Yb_{0.1}O₃ (Ni-BZCYYb) were prepared in the same manner of PBCFS01-07. The final powder of PBCFS01-07, BZCYYb, and AFL were obtained by sintering the precursor powder in a muffle furnace for 3 hours at a temperature of 1000 °C. The fuel electrode powder of NiO-BZCYYb is produced by mixing NiO, BZCYYb, and maize starch with a ratio of 60:40:20 in an alcohol solution using the ball milling technique for 24 hours. Subsequently, the mixture

A mature "fuel electrode-functional layer-electrolyte" three-layers co-sintering method was applied for manufacture of fuel electrode-supported half-cells at 1350°C for 5h. A five-millimeter-radius stainless steel module was used to press 0.36 g of anode powder to obtain the anode layer at 300 MP), followed by the sequential pressing of 0.014 g of AFL powder and 0.005 g of electrolyte powder at 200 MPa, yielding a three-layer half-point cell supported by the anode. 0.7 g of cathode powder, 0.3 g of electrolyte powder, and 10 wt% of ethylcellulose-pineol adhesive were mixed in an agate mortar and pestle to prepare the air electrode slurry. The electrolyte layer was brushed with air-electrode slurry, and the collector area was regulated to be 0.196 cm² using a fixed model. To optimize the air electrode's porosity, the air electrode slurry was coated on a dense BZCYYb electrolyte film and then dried in a vacuum furnace. The single cell was then sintered in a microwave oven at 900 °C for 10 minutes to ensure a good bond between the cathode and electrolyte layers.

Phase structures were characterized by an X-ray diffractometer (Bruker D8 advance) using Cu Kα radiation (λ=0.15406 nm, V=40 KV, I=40 mA). The surface chemical states of the PBCFS01-07 powders were examined with an X-ray photoelectron spectrometer (XPS, Thermo-Scientific K-Alpha), while the morphology and crystallinity were examined through transmission electron microscopy (TEM, FEI TF20, Super-X). Scanning electron microscopy (SEM, Phenom XL G2) was used to examine the cell microstructures.

The electrical conductivity relaxation (ECR) was applied to analyze the ORR activity of PBCFS01-07 through observing the oxygen ion adsorption and diffusion ability. Utilizing a stainless steel die and a hydraulic press, the PBCFS01-07 powders were uni-axially pressed into a cuboid bar at 250Mpa. The pressed samples were sintered at 1300 °C for 5 hours in an air atmosphere to reach a theoretical relative density of more than 95%, with a final size of roughly 3.5 mm \times 1.65 mm \times 7.5 mm. In order to automatically record the ECR behavior of the sample bars from 350 to 750°C, they were heated in a tube furnace and connected to a digital multimeter (Keithley 2010 multimeter) through four silver lead wires based on the four-probe approach. In order to determine the material's volume diffusivity and surface exchange coefficient, the gas mixture entering the alumina tube was changed from N₂:O₂=1:1 to air while maintaining the same flow rate of roughly 50 mL min⁻¹.

The assessment of hydrogen permeation flux was carried out using a custom-built apparatus. A level and parallel surface was achieved through careful preparation of the sintered PBCFS05 pellets by polishing both surfaces with SiC sandpaper. To obtain a reliable gas sealing, the pellets were securely mounted on an alumina tube using a glass ring sealant and subjected to a sealing temperature of 900 °C. The gases at the feed side were 20 mL min⁻¹ H₂ and 80 mL min⁻¹ N₂, while the sweep gas at permeate side was high purity Ar at a rate of 20 mL min⁻¹.

The proton conductivity of the materials can be obtained by the following Wagner equation:

$$\sigma_{H^{+}} = \frac{J_{H_2} \frac{4F^2L}{RT}}{ln \frac{P_{H_2 \, supp}}{P_{H_2 \, perm}}}$$

where σ_{H^+} is the proton conductivity, J_{H_2} represents the H₂ permeation flux, F is the Faraday constant which is 96 485.33 C mol⁻¹, and L represents the thicknesses of PBCFS05 (0.76 mm). R denotes the ideal gas constant, which has a value of 8.314 J (mol K)⁻¹. T represents the operating temperature in Kelvin. The variables " $P_{H_2 \ supp}$ " and " $P_{H_2 \ perm}$ " denote the hydrogen partial pressure on the hydrogen supply side and the permeate side, respectively.

Using an electrochemical apparatus (Squidstat Plus, Admiral Instruments) with a four-probe configuration, a single cell was examined. The water vapor pressure (0.03 atm) was attained by following H₂ through a water bubbler at approximately 25 °C. For the fuel cell test, 20 mL min⁻¹ of 3% H₂O-humidified H₂ was supplied to the fuel electrode as the fuel, while ambient air was supplied to the air electrode as the oxidant. For the electrolysis test, the fuel electrode was subjected to 20 mL min⁻¹ of humidified H₂ (3% H₂O), while the air electrode was supplied with 100 mL min⁻¹ of humidified (3% H₂O) air. To acquire the I-V/I-P curves of the cell, Linear Sweep Voltammetry (LSV) mode was utilized. Additionally, Electrochemical Impedance Spectra (EIS) were measured under open circuit conditions with a frequency range of 0.1-1 MHz and 10 mV as AC amplitude.

Theoretical calculations using density functional theory (DFT) were conducted on PBCFS01-07. The Vienna ab initio simulation package (VASP) was utilized with the Perdew-Burke-Ernzerhof (PBE) parametrization of the generalized gradient approximation (GGA) to incorporate electron exchange and correlation. Additionally, the Projector Augmented Wave (PAW) method was employed to represent electron waves in a pseudo potential format[32-34]. With a 4×4×4 Monkhorst-Pack type k-space grid for energy accumulation in volume and a single Gamma point for energy estimation in slab, the kinetic energy cut-off of the plane wave basis set was 500 eV, and force tolerance on each atom was set to 0.02 eV/Å for the purpose of structural relaxation calculations[35]. An illustration of the structured in Pm/3m is demonstrated in (Figure S4a, Support Information).

The bond length of the transition metal to the oxygen atom is altered when PBCF is doped with various ratios of elemental tin. The amount of oxygen vacancies in the doped material is drastically affected by this modification. Energy required for vacancy creation (E_{OV}) is determined by the following formula:

$$E_{OV} = E_{defect} + \frac{1}{2} E_{O_2} - E_{AB_3}$$
 (1)

In the formula above, E_{defect} represents the energy of the bulk with defects induced, E_{O_2} is the energy of an oxygen molecule and $E_{AB_{-3}}$ is the energy of complete bulk without defects.

Journal of Advanced Ceramics

https://mc03.manuscriptcentral.com/jacer

173 When the system's basicity rises and oxygen vacancies are produced to compensate for charge, 174 the system's charge becomes more neutral. As a result, the substance becomes more water-reactive,

which triggers the subsequent Stotz–Wagner pathway:

176
$$H_2O(g) + O_0^{\times} + V_0^{"} \to 2OH_0^{"}$$
 (2)

Hydration ability can be directly anticipated using the formula for estimating hydration energy based on the production of oxygen vacancies:

$$E_{hydration} = E_{2OH} - E_{H_2O} - E_{defect}$$
 (3)

Furthermore, proton conduction in perovskite oxides is based on two types of paths: rotation and hopping. While remaining linked to the oxygen ion, the proton spins 90° around the B-O-B axis, whereas hopping means the proton leaps from one oxygen ion to another in the same octahedron, or hops from one oxygen ion to another between distinct octahedra. The CI-NEB technique was used to determine the energetic barriers along the proton transfer pathways.

3 Results and discussion

3.1 Analysis of Composition and Structure

Analysis by X-ray diffraction (XRD) shows that as the amount of Sn dopant increases, the XRD peak shifts to lower diffraction angle (Figure 1), indicating lattice expansion in $Pr_{0.5}Ba_{0.5}Co_{0.7}Fe_{0.3-x}Sn_xO_{3-\delta}$ (x=0.01, 0.03, 0.05, and 0.07). The replacement of smaller Fe^{3+} (r =0.645 Å) or Fe^{4+} (r =0.585 Å) ions with larger Sn^{4+} (r =0.69Å) ions leads to the lattice expansion. The Goldschmidt tolerance factor ($t = \frac{(r_A + r_O)}{\sqrt{2}(r_B + r_O)}$) provides a concise explanation for the durability of ABO₃ type perovskite oxides[36]. Theoretical research reveals that t can be reduced to less than 1.0 by substituting a larger cation at B site[37]. Therefore, the creation of $Pr_{0.5}Ba_{0.5}Co_{0.7}Fe_{0.3}O_3$ with a cubic structure is favored by the replacement of smaller Fe ions with larger Sn^{4+} ions. Rietveld refinement of X ray diffraction (XRD) analysis for Sn doped $Pr_{0.5}Ba_{0.5}Co_{0.7}Fe_{0.3-x}Sn_xO_{3-\delta}$ (x=0.01, 0.03, 0.05, and 0.07) samples reveals a cubic structure with pm-3m space group symmetry, shown in Table 1 and Figure S1 (Support Information). Since B-site doping modifies the electron configuration of the B-site cations, the lattice

parameter rises in proportion to the amount of Sn doping. Furthermore, there is only one peak (110)

located near 32°, indicating that the oxygen ion transport in BO₆ octahedron is a three-dimensional

conduit that promotes oxygen reduction and oxidation reactions[38].

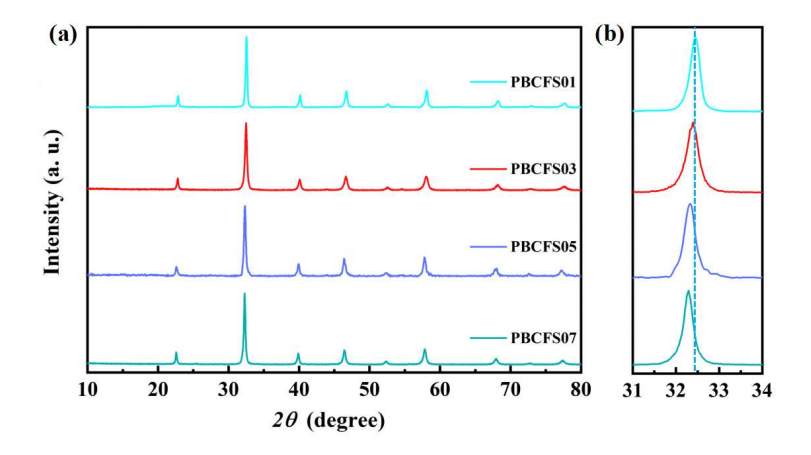


Fig. 1 XRD patterns of Sn doped $Pr_{0.5}Ba_{0.5}Co_{0.7}Fe_{0.3-x}Sn_xO_{3-\delta}$ (x=0.01, 0.03, 0.05, 0.07) powders after calcination at 1000 °C for 3h in air

Based to the STEM and energy-dispersive X-ray (EDX) images (Figure 2a-f), it can be inferred that Pr, Ba, Co, Fe, Sn and O elements are evenly dispersed. The high-resolution STEM image in Fig. 2i shows the fields-of-view of the PBCFS05 sample that was quenched at 1000 °C. In accordance with the XRD analysis, the magnified view of the targeted region in the image shows clear lattice streaks with an interplanar spacing of 0.27 nm, which can be indexed to the (110) plane of the cubic structure with space group Pm-3m. Another selected region shows the (111) plane of the cubic structure with the same space group. The FFT patterns along the [110] zone axis further support this, with the (110) and (111) lattice planes highlighted in Figure 2g-h.

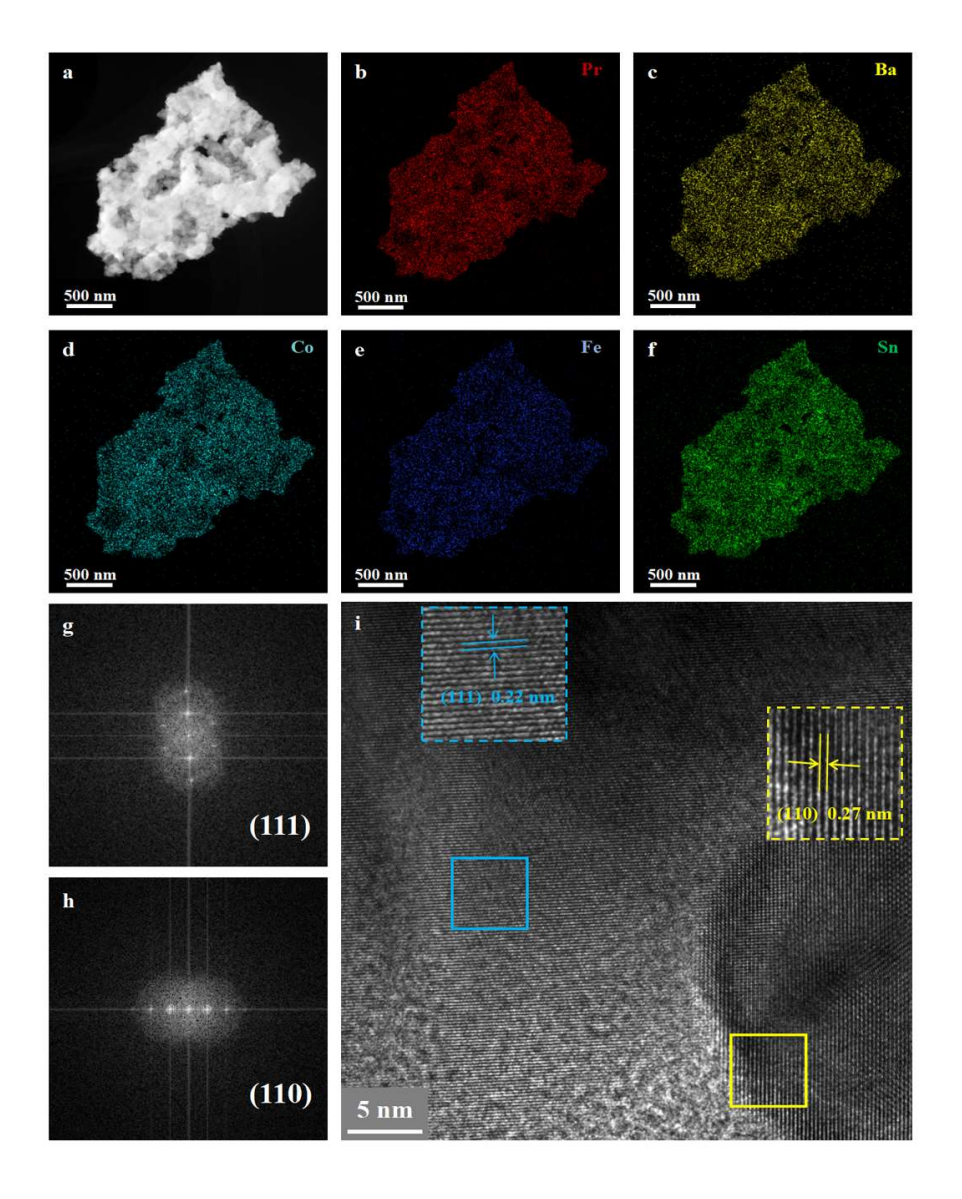


Fig. 2 Transmission electron microscopy (TEM) analysis of PBCFS05 nanoparticle and corresponding energy-dispersive X-ray spectroscopy (EDS) maps of Pr, Ba, CO, Fe and Sn

3.2 Analysis of transport properties

An air electrode material with higher electrical conductivity typically exhibits improved charge collection efficiency, lower ohmic loss, and faster charge compensation rate during the ORR process. Figure 3a shows the electrical conductivity of PBCFS01-07 measured by a DC four-probe method. The conductivity curve of PBCFS01 demonstrates a gradual increase in conductivity with increasing temperature from 350°C to 450 °C, followed by a decrease in conductivity at temperatures above 450

Journal of Advanced Ceramics https://mc03.manuscriptcentral.com/jacer °C, indicating that the conductivity of PBCFS01 changes from semiconductor-like to metallic properties at a temperature of approximately 450 °C. Comparing the conductivity curves of PBCFS01-07, the semiconductor-like nature progressively decreases and tends to be metallic between 350 °C - 450 °C as the doping content of Sn rises. Evidently, PBCFS05 almost exhibits metallic conduction between 350 °C and 750 °C. It has been reported that electronic conduction in perovskite-related oxides occurs via electron hopping along B–O–B bonds[39]. The formation of oxygen vacancies as a result of thermal reduction (Co⁴⁺/Fe⁴⁺ to Co³⁺/Fe³⁺ for cobalt-iron-based perovskite) is responsible for

the decrease in electrical conductivity with an increase in temperature [40], leading to an obstruction

of the route along which electrons travel. By analyzing the conductivity-temperature relationship, the

activation energy for electrical conduction of PBCFS05 conductivity is the lowest.

Achieving a high performance for PCFCs is also influenced by the oxygen exchange rate on the surface of the air electrodes. The electrical conductivity relaxation (ECR) method was employed to investigate the kinetic properties of the PBCFS01-07 materials (Figure 3c). The horizontal axis shows the amount of time needed for the sample to reach a new equilibrium after the ambient oxygen partial pressure was increased from 0.21 to 0.5 atm. It has been noted that the relaxation process of PBCFS05 reaches a new balance quickly, indicating a prompt reaction to the shift in P_{O_2} . The bulk diffusion coefficient (D_{chem}) and surface exchange coefficient (E_{chem}) of PBCFS01-07 at 550–700 °C were fitted according to the pure surface-controlled equilibration kinetics[41]. The specific values are listed in Table 2 (Supporting Information) and the results of the trend with temperature are summarized in Figure 3c-d. According to the D and E values for PBCFS01-07, PBCFS05 has the lowest activation energy barrier for oxygen adsorption and dissociation and for bulk conduction, which could represent an advantage for the transport of oxygen ions.

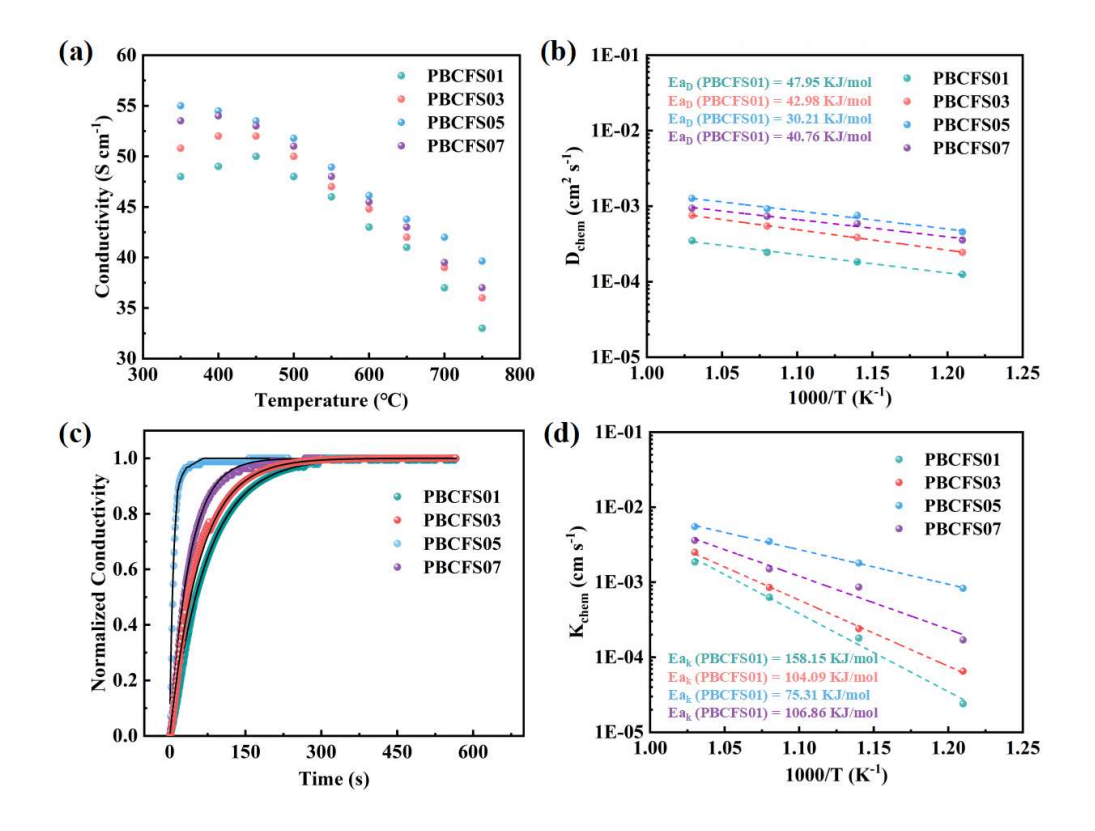


Fig. 3 Ion transfer capability of PBCFS01-07. (a) Electrical conductivities of PBCFS01-07; (b) Electrical conductivity relaxation (ECR) curves of PBCFS01-07; (c-d) The fitted values of D_{chem} and k_{chem} of PBCFS01-07 at the range of 550–700 °C, as calculated from the ECR curves

X-ray photoelectron spectroscopy (XPS) is utilized to describe the O1s core-level spectra in order to provide more insight about the chemical property of the synthesized PBCFS01-07 powders. The rate-limiting step of the cathodic oxygen reduction process is critically impacted by the surface oxygen species, which have a significant effect on the fuel cell performance. Therefore, it is crucial to search at the oxygen species present in air electrode materials. The O 1s core-level spectra are decomposed into four sections: the first is originated from the lattice oxygen O_L ; the other three contributions are attributed to the chemisorbed oxygen species (O_C) of O^{2-} , O^- , and O_2^- respectively. The fitted curve of PBCFS01-07 is depicted in the Figure 4a-d and the bond energy and the area percentage ratios of O_C/O_L are listed in Table 3 (Supporting Information). In the presence of oxygen, a sequence of

257

258

259

260

261

262

263

264

265

266

267

alterations occur on the surface of the oxide catalyst according to the general scheme[42]: $O_2 \leftrightarrow O_2$ $\xrightarrow{+e^{-}}$ $O_{2}^{-} \xrightarrow{+e^{-}}$ $O_{2}^{2^{-}} \leftrightarrow 20^{-} \xrightarrow{+2e^{-}}$ $20^{2^{-}}$ (lattice). According to the literature, the ORR activity of various air electrode materials can be evaluated using the O_C/O_L ratio as the benchmark[43]. Therefore, we can conclude from Table 3 (Supporting Information) that the value of O_C/O_L increases with increasing Sn content, indicating that Sn-doping enhances the ORR activity in the air electrode surface. For SOFCs, PBCFS05 may prove to be an effective cathode when x = 0.05, where its ORR activity is the highest. Sn^{4+} produces lone pair electrons, which assists the oxygen ions bound to it easily to escape from the crystal lattice forming more oxygen vacancies[44].

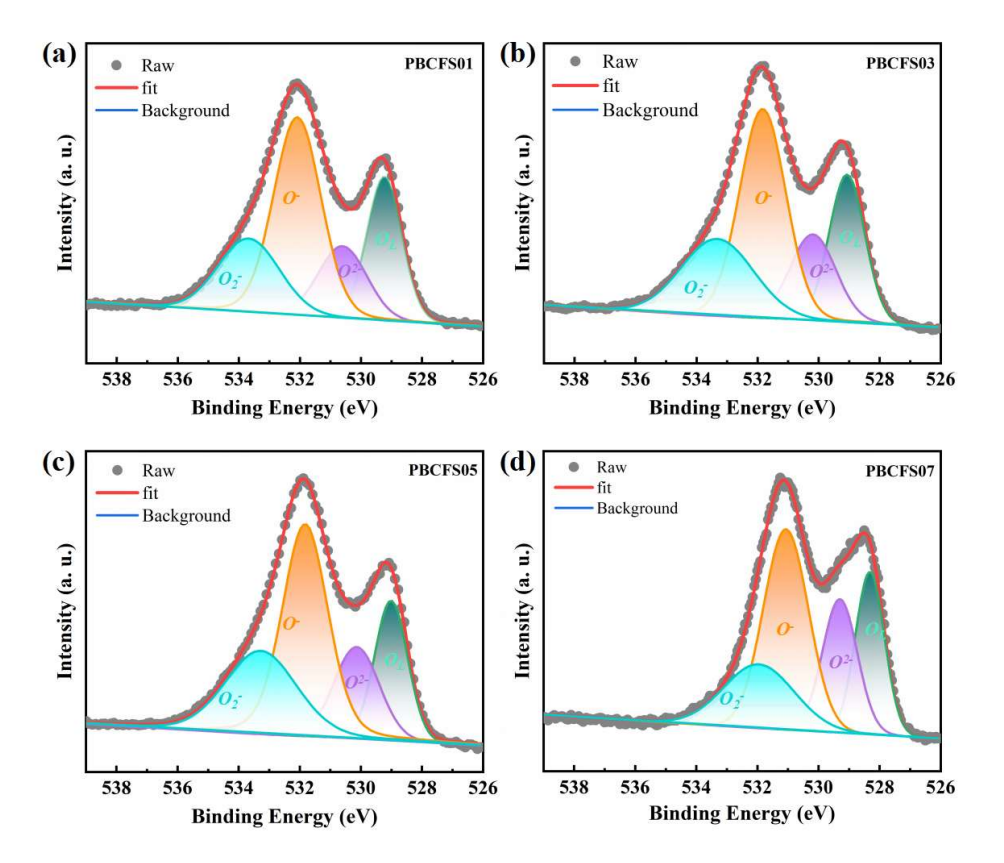


Fig. 4 O1s core-level spectra of PBCFS01-07 at room temperature (the red line shows the fitting results).

3.3 Theoretical calculation

It is crucial to reveal the reaction mechanism and identify the basic steps of the electrochemical reaction at the cathode for PCFC in order to better understand the cathode process. The enthalpy of the reaction can be determined by calculating the energies of the complete lattice, the defective lattice, and the oxygen molecules in gas phase. In the complete lattice of PBCFS05, there is an oxygen (O_0^\times) located between two transition metal ions (M_M^\times) , whereas in the defective lattice, there is an oxygen vacancy (V_0^\times) accompanied by two adjacent reduced metal sites (M_M^\prime) . Defective PBCFS05 lattices are formed when a neutral oxygen atom is removed, resulting in the creation of a V_0^\times , and the degree of non-stoichiometry (δ) depends on the size of the periodic supercell model. From the description in KrÖger-Vink reaction, the formation of an oxygen vacancy can be expressed according to the following equation:

$$2M_{M}^{\times} + O_{O}^{\times} \to 2M_{M}' + V_{O}^{"} + \frac{1}{2}O_{2}(g)$$
 (4)

By calculating the oxygen vacancy formation energy of various oxygen sites (summarized in Table 4, Support Information), it can be concluded that the optimal oxygen vacancy site is located between the Fe and Co atoms on the Co-Fe-Sn-O plane and has an energy of -3.6 eV (Figure S4b, Support Information). Upon the removal of an oxygen atom from the complete lattice by breaking two Co-O-Fe bonds, redistribution of two electrons associated with the neutral O²⁻ ion occurs within the defective crystal. The thermodynamics of V₀ formation depends on various factors such as the strength of the M-O-M bond and the electron magnetization of two neighboring M ions that transform from a highly charged to a less charged configuration[45, 46]. Calculations indicate that doping Sn weakens adjacent Co-O bond energy and increases electron magnetization in Co-O-Fe.

To further demonstrate the introduction of protons by Sn doping, theoretical studies based on a well-established model are conducted to examine the impact of Sn-doping on the hydration capacity of the material. After selecting the appropriate oxygen ions, the surrounding proton energy landscape was analyzed so that the protons occupied the positions with the lowest energy. The calculated hydration energy for PBCFS05 is 0.65 eV, lower than PBCF[47]. On the basis of Coulombic repulsion

Journal of Advanced Ceramics https://mc03.manuscriptcentral.com/jacer alone, one might anticipate that the introduction of Sn into the PBCF system would result in an enhancement in its hydration capacity. Additionally, the importance of basicity in assessing the hydration capacity of such materials has been established[48, 49].

Proton transfer typically takes two routes based on "Grotthuss-type" mechanism, shown in Figure S5c and Figure S6 (Supporting Information): reorientation and intra-octahedral hopping. The energy barriers of proton reorientation and intra-octahedral hopping were calculated by the NEB method. For reorientations with the lowest energies of -0.0803eV [O21(a) to O21(b)], the proton is migrating to a location that is either closer to the Sn ion or further from the Fe ion. For the possible intra-octahedral hopping, it has been found that protons transferring across the path of O21-O18 require the lowest energy, only -0.11035 eV. The DFT results indicate that transporting protons is simpler in PBCFS05 than PBCF because the barrier energies for the hopping and rotating processes are lower. To enhance the verification of proton conductivity in PBCFS05, hydrogen permeation tests were conducted on pellets of PBCFS05, as depicted in Figure S7 (Supporting Information). The proton conductivity of PBCFS05 in discussion exhibits a level of comparability to that of other related materials[50].

3.4 Electrochemical performance in the fuel cell mode

Figure 5a displays representative cross-sectional SEM images of the single cells composed of Ni-BZCYYb1711 fuel electrode, AFL, dense BZCYYb1711 electrolyte (6-7 μ m), and the PBCFS05 air electrode after electrochemical performance test. To investigate the impact of Sn doping levels on electrochemical behaviour, fuel electrode-supported SOFCs with PBCFS01-07 cathodes are tested at 700 °C. As shown in Figure 5b, maximum power densities (MPDs) of 1225, 1332, 1644, and 1416 mW cm⁻² are achieved by fuel cells with PBCFS01, PBCFS03, PBCFS05 and PBCFS07 air electrode, respectively. The corresponding polarization resistances are shown in Figure 5c to evaluate the air electrode reaction process. At 700 °C, PBCFS05 has the lowest polarization resistance of 0.029 Ω cm², while PBCFS01 has the highest polarization resistance of 0.05 Ω cm². Moreover, fuel cells with PBCFS01-07 retain their advantageous electrochemical performance even at the operating

temperatures down to 600 °C. Figure 5d shows that PBCFS05 exhibits the highest catalytic activity of 318 ORR at 600 °C with a MPD of 1122 mW cm⁻², while the MPDs of fuel cells with PBCFS01, PBCFS03, 319 and PBCFS07 measured at 600 °C is 640 mW cm⁻², 710 mW cm⁻², and 864 mW cm⁻² respectively. 320 The polarization resistance of PBCFS05, PBCFS01, PBCFS03, and PBCFS07 at 600 °C is 0.09Ω cm², 321 $0.23~\Omega~cm^2$, $0.16~\Omega~cm^2$, and $0.14~\Omega~cm^2$, respectively. Distribution of relaxation time (DRT) analysis 322 323 of EIS data obtained at 600 °C aids in the comprehensive analysis for the kinetics of electrode 324 reactions. The DRT maps can be categorized into peaks that are distributed at low (LF, less than 10 Hz), intermediate (IF, 10–2000 Hz), and high frequencies (HF, more than 2,000 Hz). These peaks are 325 typically associated with gas diffusion processes, surface oxygen exchange processes, and charge 326 327 transfer processes, respectively[51]. From Figure 5f, the PBCFS05 electrode's much narrower IF peak 328 compared to the other samples suggests an exceptionally efficient surface oxygen exchange 329 mechanism (consisting of oxygen adsorption/desorption at the electrode surface, dissociation of 330 oxygen at the surface, and diffusion)[52]. This is in accordance with the ECR results displayed in Figure 3c and the related electrode reactions are detailed below: 331 Oxygen adsorption and dissociation: $O_2(g)+PBCFS05\rightarrow 2O_{ad}(PBCFS05)$ 332 Oxygen reduction: O_{ad} (PBCFS05) $+e^- \rightarrow O^-$ (PBCFS05) $/ O^-$ (PBCFS05) $+e^- \rightarrow O^{2-}$ (PBCFS05) 333 Surface diffusion: $O^{2-}(PBCFS05) \rightarrow O^{2-}(TPB)$ 334 Figure 5g is a summary of the MPDs of fuel cells that were evaluated at temperatures ranging 335 from 550 °C to 700 °C. The graph indicates that PBCFS05 outperforms other air electrodes at every 336 337 temperature point, showcasing its advantages over other materials in fuel cell applications. In addition, the relatively low Ea (as shown in Figure 5h) and the lowest electrode polarization resistance 338 collectively demonstrate the superiority of PBCFS05 cathode. Lastly, the cell operates continuously 339 340 for over 100 hours with relatively stable performance (displayed in Figure 5i). Consequently,

PBCFS05 could be a potential air electrode for PCFC due to its high PPDs, low R_P and good durability

https://mc03.manuscriptcentral.com/jacer

Journal of Advanced Ceramics

341

342

under comparable conditions.

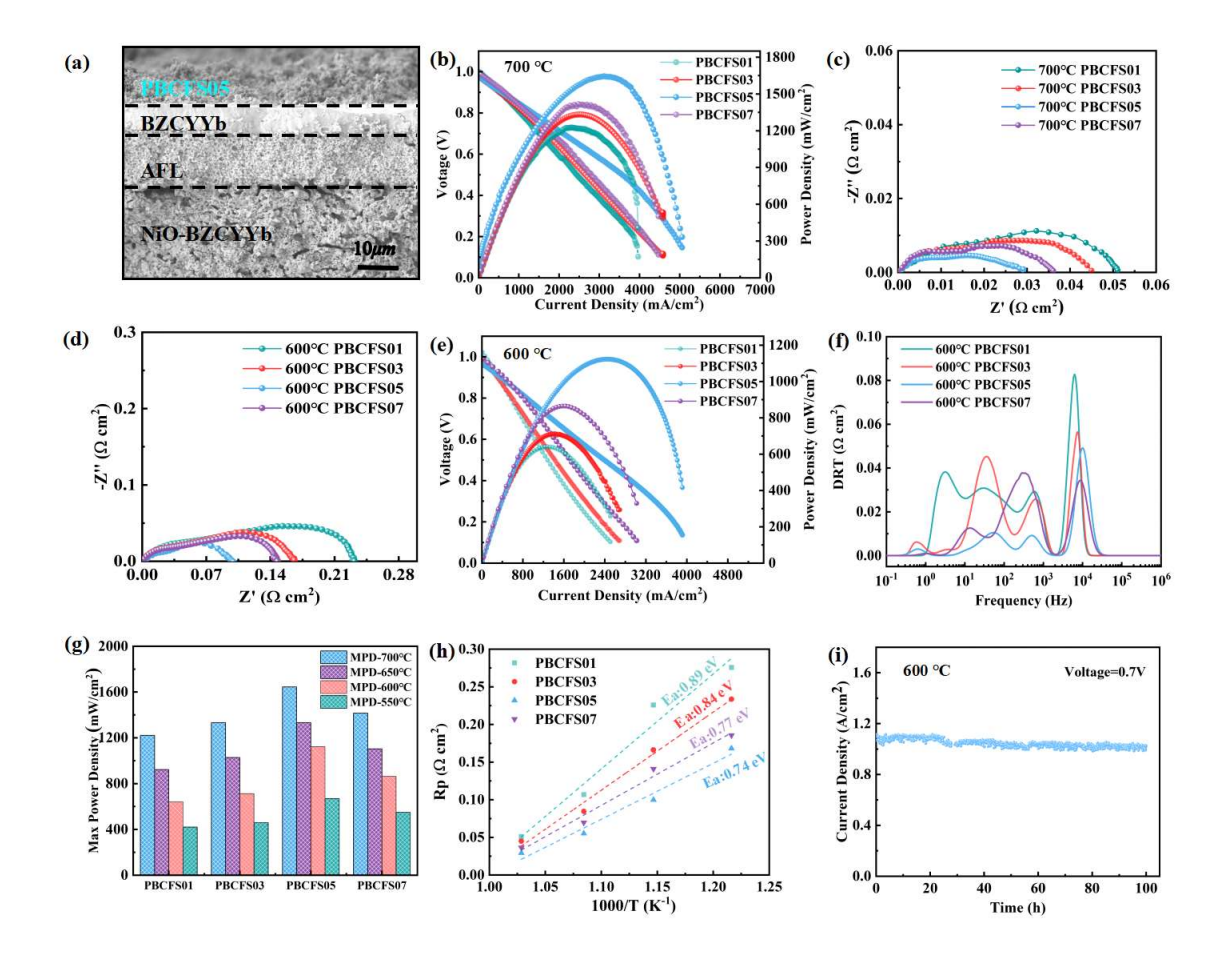
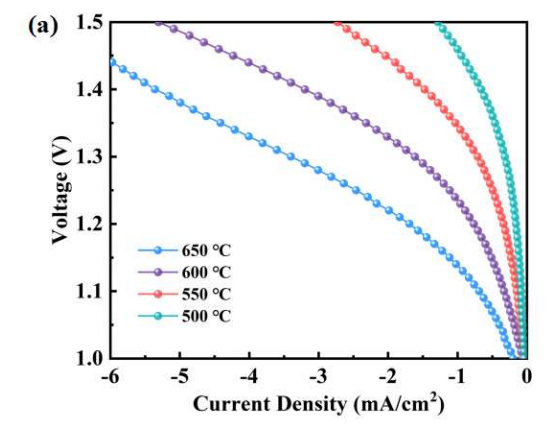


Fig. 5 Performance of the fuel cells with PBCFS01-07 as the air electrode. (a) Cross-sectional SEM image of a single cell; (b) I-V and I-P curves of fuel cells with different ratio of Sn doped PBCFS01-07 electrodes measured at 700 °C; (c) EIS curves of fuel cells with different ratio of Sn doped PBCFS01-07 electrodes measured at 700 °C; (d) I-V and I-P curves of fuel cells with PBCFS01-07 electrodes measured at 600 °C; (e) EIS curves of fuel cells with PBCFS01-07 electrodes measured at 600 °C; (f) DRT analysis of the EIS data measured at 600 °C; (g) Comparison of MPD for fuel cells with different ratio of Sn doped PBCFS01-07 electrodes tested at 550 °C to 700 °C; (h) Comparison of R_P for fuel cells with different ratio of Sn doped PBCFS01-07 electrodes tested from 550 °C to 700 °C; (i) Operation stability test of a fuel cell with PBCFS05 cathode under a constant voltage of 0.7 V at 600 °C.

3.5 Performance and stability in the electrolysis mode

The electrochemical performance of R-PCEC with PBCFS05 as the air electrode was also evaluated in the electrolysis mode, with the I-V plots at 550-650 °C shown in Figure 6a, and 3.56 A cm⁻², 1.79 A cm⁻², 0.75 A cm⁻², and 0.33 A cm⁻² were the corresponding current densities at a cell voltage of 1.3 V for temperatures at 650, 600, 550, and 500 °C, respectively. Figure 6b depicts the cell current as a function of time of R-PCEC using PBCFS05 as the air electrode. The experimental conditions were operating the cell in both fuel cell and electrolysis modes at a temperature of 600 °C. The cyclic operation consisted of switching the cell voltage from 1.3V to 0.7V and maintaining each voltage level for a duration of 4 hours in both modes. The entire cyclic testing lasted for 100 hours (for a total of 13 cycles), and a stable operation was observed, indicating an excellent reversibility of the PCECs

R-PCECs with PBCFS05 as the air electrode exhibit comparable, if not superior, performance relative to the majority of current state-of-the-art R-PCECs. It is evident in both the fuel cell mode, where they exhibit high peak power density, and the electrolysis mode, where they achieve significant current density at 1.3 V. This information is supported by the Figure 7 and the supplementary Table 7-8. Moreover, R-PCECs with PBCFS05 as the air electrode have shown excellent durability in the reversible operation in both the fuel cell and electrolysis mode (Figure 6b), demonstrating that PBCFS05 is an outstanding air electrode for both the oxygen reduction reaction and the oxygen evolution reaction.



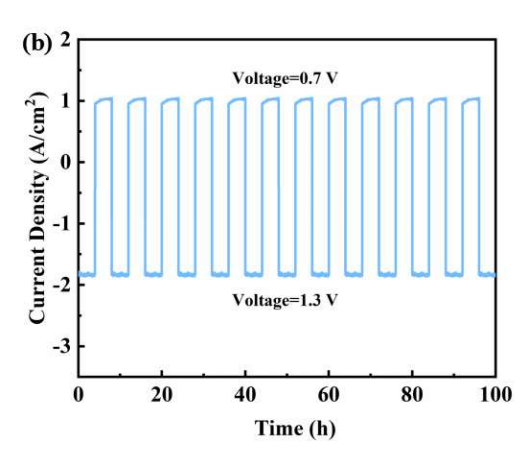


Fig. 6 (a) Electrochemical performance of R-PCECs with PBCFS05 as the air electrode in electrolysis mode; (b) Reversible operation of the R-PCEC: the cell voltage was switched from 0.7V in the fuel

cell to 1.3V in the electrolysis modes at 600 °C.

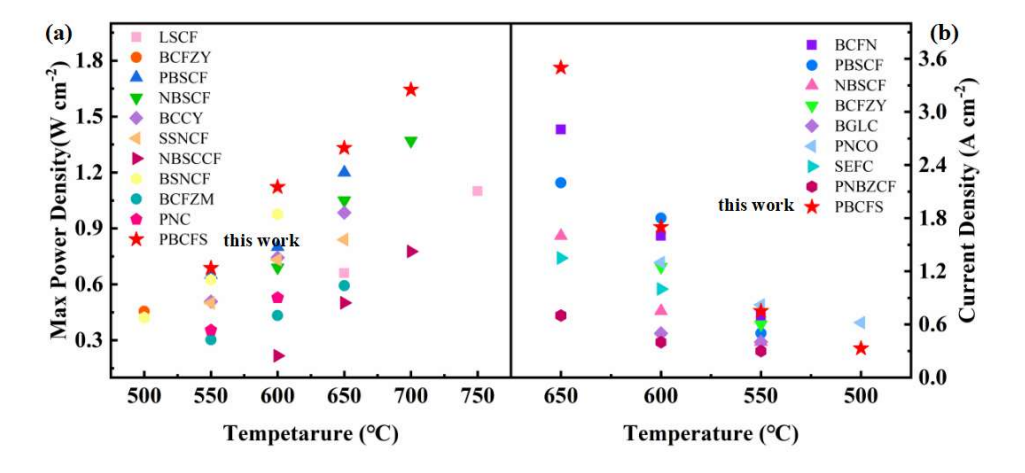


Fig. 7 Performance comparison of the state-of-the-art R-PCECs. (a) MPD in the fuel cell mode; (b) Current density comparison at 1.3V in the electrolysis mode.

4 Conclusion

This study reports Sn-doping on the B-site, Pr_{0.5}Ba_{0.5}Co_{0.7}Fe_{0.3-x}Sn_xO_{3-δ} as the air electrode for R-PCEC applications. At 600 °C, single cells using PBCFS05 as the air electrode demonstrated a maximum power density of 1.12 W cm⁻² in the fuel cell mode and a current density of 1.79 A cm⁻² at 1.3V in the electrolysis mode, outperforming the majority of R-PCEC using other air electrode materials. In addition, fuel cells using PBCFS05 as air electrode cells exhibited reasonable stability during operation at 0.7V in the fuel cell mode for 100 hours and an excellent reversible cell performance for a total of 13 cycles in the fuel cell (V=0.7V) and the electrolysis (V=1.3V) mode. The rational and effective design of PBCFS05 has been shown to have potential as a promising air electrode for application in R-PCECs, with high cell performance and good long-term stability.

Acknowledgements

- Journal of Advanced Ceramics https://mc03.manuscriptcentral.com/jacer
- This work was financially supported by the National Natural Science Foundation of China (Grant Nos.:
- 392 11875164), Natural Science Foundation of the Higher Education Institutions of Jiangsu Province (No.
- 393 18KJA430017) and U.S. National Science Foundation (1832809).

394 **Declaration of competing interest**

The authors have no competing interests to declare that are relevant to the content of this article.

396 Electronic Supplementary Material (ESM)

397 Supplementary material is available in the online version of this article.

398 **References**

- 399 [1] Xu K, Zhang H, Xu YS, He F, Zhou YC, Pan YX, et al. An Efficient Steam-Induced
- Heterostructured Air Electrode for Protonic Ceramic Electrochemical Cells. Advanced
- 401 Functional Materials. 2022;32:2110998.
- 402 [2] Zhang Y, Shen L, Wang Y, Du Z, Zhang B, Ciucci F, et al. Enhanced oxygen reduction kinetics of
- IT-SOFC cathode with $PrBaCo_2O_{5+\delta}/Gd_{0.1}Ce_{1.9}O_{2-\delta}$ coherent interface. Journal of Materials
- 404 Chemistry A. 2022;10:3495-505.
- 405 [3] Ndubuisi A, Abouali S, Singh K, Thangadurai V. Recent advances, practical challenges, and
- 406 perspectives of intermediate temperature solid oxide fuel cell cathodes. Journal of Materials
- 407 Chemistry A. 2022;10:2196-227.
- 408 [4] Pei K, Zhou Y, Xu K, Zhang H, Ding Y, Zhao B, et al. Surface restructuring of a perovskite-type
- 409 air electrode for reversible protonic ceramic electrochemical cells. Nature Communications.
- 410 2022;13:2207.
- 411 [5] Duan C, Kee R, Zhu H, Sullivan N, Zhu L, Bian L, et al. Highly efficient reversible protonic
- 412 ceramic electrochemical cells for power generation and fuel production. Nature Energy.
- 413 2019;4:230-40.
- 414 [6] Ding H, Wu W, Jiang C, Ding Y, Bian W, Hu B, et al. Self-sustainable protonic ceramic
- 415 electrochemical cells using a triple conducting electrode for hydrogen and power production.
- Nature communications. 2020;11:1907.
- 417 [7] Hu T, Zhu F, Xia J, He F, Du Z, Zhou Y, et al. In Situ Engineering of a Cobalt-free Perovskite Air
- Electrode Enabling Efficient Reversible Oxygen Reduction/evolution Reactions. Advanced
- 419 Functional Materials. 2023:2305567.

- Journal of Advanced Ceramics https://mc03.manuscriptcentral.com/jacer
- 420 [8] He F, Liu S, Wu T, Yang MT, Li WH, Yang GM, et al. Catalytic Self-Assembled Air Electrode
- for Highly Active and Durable Reversible Protonic Ceramic Electrochemical Cells. Advanced
- Functional Materials. 2022;32:10.
- 423 [9] Rajendran S, Thangavel NK, Ding HP, Ding Y, Ding D, Arava LMR. Tri-Doped BaCeO₃-BaZrO₃
- as a Chemically Stable Electrolyte with High Proton-Conductivity for Intermediate Temperature
- Solid Oxide Electrolysis Cells (SOECs). Acs Applied Materials & Interfaces. 2020;12:38275-84.
- 426 [10] Leonard K, Okuyama Y, Takamura Y, Lee Y S, Miyazaki K, Ivanova ME, et al. Efficient
- 427 intermediate-temperature steam electrolysis with Y: SrZrO₃–SrCeO₃ and Y: BaZrO₃–BaCeO₃
- proton conducting perovskites. Journal of Materials Chemistry A. 2018;6:19113-24.
- 429 [11] Wang WJ, Li YT, Liu Y, Tian YF, Ma B, Li J, et al. Ruddlesden-Popper-Structured
- 430 (Pr_{0.9}La_{0.1})₍₂₎(Ni_{0.8}Cu_{0.2})O_{4+δ}: An Effective Oxygen Electrode Material for Proton-Conducting
- Solid Oxide Electrolysis Cells. Acs Sustainable Chemistry & Engineering. 2021;9:10913-9.
- [12] Kim J, Sengodan S, Kim S, Kwon O, Bu Y, Kim G. Proton conducting oxides: A review of
- 433 materials and applications for renewable energy conversion and storage. Renewable and
- Sustainable Energy Reviews. 2019;109:606-18.
- [13] Duan C, Tong J, Shang M, Nikodemski S, Sanders M, Ricote S, et al. Readily processed protonic
- ceramic fuel cells with high performance at low temperatures. Science. 2015;349:1321-6.
- 437 [14] Xu YS, Xu X, Bi L. A high-entropy spinel ceramic oxide as the cathode for proton-conducting
- 438 solid oxide fuel cells. Journal of Advanced Ceramics. 2022;11:794-804.
- 439 [15] Xu K, Pei K, Zhao B, Zhao Y, Niu Q, Chen Y. An oxygen reduction reaction active and durable
- 440 SOFC cathode/electrolyte interface achieved via a cost-effective spray-coating. International
- 441 Journal of Hydrogen Energy. 2021;46:32242-9.
- 442 [16] Fabbri E, Bi L, Pergolesi D, Traversa E. High-performance composite cathodes with tailored
- 443 mixed conductivity for intermediate temperature solid oxide fuel cells using proton conducting
- electrolytes. Energy & Environmental Science. 2011;4:4984-93.
- [17] Rao Y, Zhong S, He F, Wang Z, Peng R, Lu Y. Cobalt-doped BaZrO₃: A single phase air electrode
- material for reversible solid oxide cells. International journal of hydrogen energy. 2012;37:12522-
- 447 7.
- 448 [18] Mather GC, Muñoz-Gil D, Zamudio-García J, Porras-Vázquez JM, Marrero-López D, Pérez-Coll
- D. Perspectives on cathodes for protonic ceramic fuel cells. Applied Sciences. 2021;11:5363.
- 450 [19] Shen M, Ai F, Ma H, Xu H, Zhang Y. Progress and prospects of reversible solid oxide fuel cell
- 451 materials. Iscience. 2021;24.

Journal of Advanced Ceramics

- https://mc03.manuscriptcentral.com/jacer
- 452 [20] Grimaud A, Mauvy F, Bassat J, Fourcade S, Rocheron L, Marrony M, et al. Hydration properties
- and rate determining steps of the oxygen reduction reaction of perovskite-related oxides as H⁺-
- SOFC cathodes. Journal of The Electrochemical Society. 2012;159:B683.
- 455 [21] Yin YR, Zhou YB, Gu YY, Bi L. Successful preparation of BaCo_{0.5}Fe_{0.5}O_{3-δ} cathode oxide by
- rapidly cooling allowing for high-performance proton-conducting solid oxide fuel cells. Journal
- 457 of Advanced Ceramics. 2023;12:587-97.
- 458 [22] Ding H, Xue X. Proton conducting solid oxide fuel cells with layered PrBa_{0.5}Sr_{0.5}Co₂O_{5+δ}
- 459 perovskite cathode. international journal of hydrogen energy. 2010;35:2486-90.
- 460 [23] Kim J, Sengodan S, Kwon G, Ding D, Shin J, Liu M, et al. Triple-conducting layered perovskites
- as cathode materials for proton-conducting solid oxide fuel cells. ChemSusChem. 2014;7:2811-
- 462 5.
- 463 [24] Qiu P, Liu B, Wu L, Qi HY, Tu BF, Li J, et al. K-doped BaCo_{0.4}Fe_{0.4}Zr_{0.2}O_{3-δ} as a promising
- cathode material for protonic ceramic fuel cells. Journal of Advanced Ceramics. 2022;11:1988-
- 465 2000.
- 466 [25] Zhang Y, Chen B, Guan D, Xu M, Ran R, Ni M, et al. Thermal-expansion offset for high-
- performance fuel cell cathodes. Nature. 2021;591:246-51.
- 468 [26] Jin F, Li J, Wang Y, Chu X, Xu M, Zhai Y, et al. Evaluation of Fe and Mn co-doped layered
- perovskite $PrBaCo_{2/3}Fe_{2/3}Mn_{1/2}O_{5+\delta}$ as a novel cathode for intermediate-temperature solid-oxide
- fuel cell. Ceramics International. 2018;44:22489-96.
- 471 [27] Shabri HA, Othman MHD, Mohamed MA, Kurniawan TA, Jamil SM. Recent progress in metal-
- 472 ceramic anode of solid oxide fuel cell for direct hydrocarbon fuel utilization: A review. Fuel
- 473 Processing Technology. 2021;212:106626.
- 474 [28] Takenaka K, Inoue N, Mizuno Y, Okamoto Y, Katayama N, Sakai Y, et al. Extended operating
- temperature window of giant negative thermal expansion in Sn-doped Ca₂RuO₄. Applied Physics
- 476 Letters. 2018;113:071902.
- 477 [29] Zvonareva IA, Mineev AM, Tarasova NA, Fu XZ, Medvedev DA. High-temperature transport
- 478 properties of $BaSn_{1-x}Sc_xO_{3-\delta}$ ceramic materials as promising electrolytes for protonic ceramic fuel
- cells. Journal of Advanced Ceramics. 2022;11:1131-43.
- 480 [30] Xia Y, Jin Z, Wang H, Gong Z, Lv H, Peng R, et al. A novel cobalt-free cathode with triple-
- 481 conduction for proton-conducting solid oxide fuel cells with unprecedented performance. Journal
- of Materials Chemistry A. 2019;7:16136-48.
- 483 [31] Xia W, Li Q, Sun L, Huo L, Zhao H. Electrochemical performance of Sn-doped Bi_{0.5}Sr_{0.5}FeO_{3-δ}
- perovskite as cathode electrocatalyst for solid oxide fuel cells. Journal of Alloys and Compounds.
- 485 2020;835:155406.

Journal of Advanced Ceramics

- https://mc03.manuscriptcentral.com/jacer
- 486 [32] Kresse G, Furthmüller J. Efficient iterative schemes for ab initio total-energy calculations using
- a plane-wave basis set. Physical review B. 1996;54:11169.
- 488 [33] Blöchl PE. Projector augmented-wave method. Physical review B. 1994;50:17953.
- 489 [34] Perdew JP, Burke K, Ernzerhof M. Generalized gradient approximation made simple. Physical
- 490 review letters. 1996;77:3865.
- 491 [35] Monkhorst HJ, Pack JD. Special points for Brillouin-zone integrations. Physical review B.
- 492 1976;13:5188.
- 493 [36] Pena M, Fierro J. Chemical structures and performance of perovskite oxides. Chemical reviews.
- 494 2001;101:1981-2018.
- 495 [37] Kida T, Takauchi D, Watanabe K, Yuasa M, Shimanoe K, Teraoka Y, et al. Oxygen permeation
- 496 properties of partially A-site substituted BaFeO_{3-δ} perovskites. Journal of The Electrochemical
- 497 Society. 2009;156:E187.
- 498 [38] Chen Y-C, Yashima M, Ohta T, Ohoyama K, Yamamoto S. Crystal structure, oxygen deficiency,
- and oxygen diffusion path of perovskite-type lanthanum cobaltites La_{0.4}Ba_{0.6}CoO_{3-δ} and
- La_{0.6}Sr_{0.4}CoO_{3- δ}. The Journal of Physical Chemistry C. 2012;116:5246-54.
- 501 [39] Zhang K, Ge L, Ran R, Shao Z, Liu S. Synthesis, characterization and evaluation of cation-ordered
- 502 LnBaCo₂O_{5+δ} as materials of oxygen permeation membranes and cathodes of SOFCs. Acta
- 503 Materialia. 2008;56:4876-89.
- 504 [40] Jin F, Liu X, Chu X, Shen Y, Li J. Effect of nonequivalent substitution of Pr^{3+/4+} with Ca²⁺ in
- PrBaCoFeO_{5+δ} as cathodes for IT-SOFC. Journal of Materials Science. 2021;56:1147-61.
- 506 [41] Wang Y, Hu B, Zhu Z, Bouwmeester HJ, Xia C. Electrical conductivity relaxation of
- 507 Sr₂Fe_{1.5}Mo_{0.5}O_{6-δ}-Sm_{0.2}Ce_{0.8}O_{1.9} dual-phase composites. Journal of Materials Chemistry A.
- 508 2014;2:136-43.
- 509 [42] Merino NA, Barbero BP, Eloy P, Cadús LE. La_{1-x}Ca_xCoO₃ perovskite-type oxides: Identification
- of the surface oxygen species by XPS. Applied Surface Science. 2006;253:1489-93.
- 511 [43] Liu M, Gao J, Liu X, Meng G. High performance of anode supported BaZr_{0.1}Ce_{0.7}Y_{0.2}O_{3-δ}
- 512 (BZCY) electrolyte cell for IT-SOFC. International journal of hydrogen energy. 2011;36:13741-
- 513 5.
- 514 [44] Dadyburjor DB, Ruckenstein E. Activation energies to characterize ease of removal of various
- kinds of oxygen from bismuth molybdate. Journal of Catalysis. 1980;63:383-8.
- 516 [45] Tang W, Sanville E, Henkelman G. A grid-based Bader analysis algorithm without lattice bias.
- Journal of Physics: Condensed Matter. 2009;21:084204.
- [46] Carter EA, Goddard III WA. Early-versus late-transition-metal-oxo bonds: the electronic structure
- of oxovanadium⁽¹⁺⁾ and oxoruthenium⁽¹⁺⁾. The Journal of Physical Chemistry. 1988;92:2109-15.

Journal of Advanced Ceramics	https://mc03.manuscriptcentral.com/jace
------------------------------	---

- 520 [47] Tao Z, Fu M, Liu Y, Gao Y, Tong H, Hu W, et al. High-performing proton-conducting solid oxide
- fuel cells with triple-conducting cathode of $Pr_{0.5}Ba_{0.5}(Co_{0.7}Fe_{0.3})O_{3-\delta}$ tailored with W.
- International Journal of Hydrogen Energy. 2022;47:1947-53.
- 523 [48] Kreuer K-D, Münch W, Fuchs A, Klock U, Maier J. Proton conducting alkaline earth zirconates
- and titanates for high drain electrochemical applications. Solid State Ionics. 2001;145:295-306.
- [49] Kreuer K. Aspects of the formation and mobility of protonic charge carriers and the stability of perovskite-type oxides. Solid State Ionics. 1999;125:285-302.
- 527 [50] Yin Y, Xiao D, Wu S, Da'as EH, Gu Y, Bi L. A real proton-conductive, robust, and cobalt-free
- 528 cathode for proton-conducting solid oxide fuel cells with exceptional performance. SusMat.
- 529 2023;3:697-708.

- 530 [51] Shi N, Su F, Huan D, Xie Y, Lin J, Tan W, et al. Performance and DRT analysis of P-SOFCs
- fabricated using new phase inversion combined tape casting technology. Journal of Materials
- 532 Chemistry A. 2017;5:19664-71.
- 533 [52] Chen Y, Choi Y, Yoo S, Ding Y, Yan R, Pei K, et al. A highly efficient multi-phase catalyst
- dramatically enhances the rate of oxygen reduction. Joule. 2018;2:938-49.